



Modelling heat and mass transfer in solar evaporation systems

R. Fillet, V. Nicolas, V. Fierro, A. Celzard

► To cite this version:

R. Fillet, V. Nicolas, V. Fierro, A. Celzard. Modelling heat and mass transfer in solar evaporation systems. International Journal of Heat and Mass Transfer, In press, 181, pp.121852. 10.1016/j.ijheatmasstransfer.2021.121852 . hal-03450059

HAL Id: hal-03450059

<https://hal.univ-lorraine.fr/hal-03450059>

Submitted on 25 Nov 2021

HAL is a multi-disciplinary open access archive for the deposit and dissemination of scientific research documents, whether they are published or not. The documents may come from teaching and research institutions in France or abroad, or from public or private research centers.

L'archive ouverte pluridisciplinaire **HAL**, est destinée au dépôt et à la diffusion de documents scientifiques de niveau recherche, publiés ou non, émanant des établissements d'enseignement et de recherche français ou étrangers, des laboratoires publics ou privés.



Distributed under a Creative Commons Attribution - NonCommercial - NoDerivatives 4.0 International License

1

Modelling heat and mass transfer in 2 solar evaporation systems

3 R. Fillet, V. Nicolas^{*}, V. Fierro, A. Celzard^{*}

4

5 Université de Lorraine, CNRS, IJL, F-88000 Epinal, France

6

7

8 ***Corresponding Author:** vincent.nicolas@univ-lorraine.fr

9 ***Corresponding Author:** alain.celzard@univ-lorraine.fr

10

11 **Abstract**

12 A two-dimensional axisymmetric model of a solar evaporator was developed, based on a
13 rigid biosourced open-cell foam floating on the surface of water contained in a beaker,
14 including a set of boundary conditions and water transport in the porous medium.
15 Experiments were carried out to validate the model for two cases, with and without a layer of
16 insulating material around the beaker. Several concrete cases of experimental solar
17 evaporation studies recently reported in the literature, with or without insulation, radiation
18 intensification, etc., have then been studied in the light of our model. We have thus been able
19 to compare the observed trends with those of the numerical model in order to explain the
20 results reported in the literature and, in some cases, to find a geometric optimum. The effect
21 of ambient conditions on the evaporation rate was investigated, and significant changes were
22 observed by modifying solar input, air temperature and air humidity. We also showed that
23 increasing the evaporation area and using an insulating layer between the water and the
24 evaporative material increases the evaporation performance.

25

26

27

28 **Keywords:** Simulation, Biosourced material, Solar energy, Solar evaporation, Porous media,
29 Heat and mass transfers

30

31 **1 Introduction**

32 In modern society, energy plays a major role, and its development as we know it today is
33 only possible with access to a significant amount of resources. Nowadays, improving the
34 effectiveness of systems and producing energy from more sustainable sources is more
35 relevant than ever. Water evaporation, for example, is a subject of great interest [1] and a
36 wide variety of materials have recently been developed to produce clean water from any
37 source, even polluted water and seawater, without the need for an energy grid. Evaporation
38 indeed occurs with or without solar flux at the water surface, but it can be enhanced by adding
39 a floating porous medium.

40 Water evaporation systems (WESs) are composed of one or more materials, sometimes
41 synthesised or manufactured from a natural resource, whose characteristics can be modified to
42 improve evaporation efficiency [2]. In general, studies aim to improve materials properties,
43 *e.g.* to increase the absorption of sunlight, to improve the energy conversion of light into heat
44 or to improve the transport of water to the surface. Thermal conductivity can also be modified
45 to reduce transfer to bulk water and thus conserve energy at the surface where evaporation
46 occurs. In addition, the resistance of materials to clogging has been studied in seawater
47 evaporation processes, where salt can affect long-term performance [3]. Changes in geometry
48 have also been made to exploit heat exchange from the air to the surface instead of letting the
49 transfer occur from the hot evaporation surface to the air [4].

50 Besides the large variability of solar evaporation systems mentioned above, a common
51 problem encountered when reading the literature is that the protocol for measuring
52 experimental performance is not identical in all publications. For example, some studies
53 report mass loss measurements under a transparent bell jar and others do not. The bell jar has
54 the effect of increasing the temperature and humidity of the air around the material compared
55 to an open air system. In addition, tests can be carried out in different locations around the

56 world with different humidity and temperature conditions. In some cases, an insulating layer
57 can be used to support the evaporation material, which would not necessarily be able to float
58 on its own, and to provide thermal insulation with the bulk water. Examples of such a system
59 have been published based on pomelo peal [5] or plant stems [6]. All of these differences lead
60 to more or less favourable conditions for the evaporation of water, regardless of the material.

61 The interest in proposing a numerical model that takes into account the mass and heat
62 transfer that underlies water evaporation is the ability to accurately capture the behaviour of
63 such WESs, and to explore the effect of experimental parameters such as those presented
64 above. Whether it is the layout of the system, the geometry of the material or even the
65 properties of the water within the material, it is possible to examine all of these impacts on the
66 overall performance and behaviour in order to better understand how to design an efficient
67 evaporation system. Furthermore, although numerical simulations have been used in the past
68 for solar evaporation systems, they were limited to predicting certain aspects such as
69 temperature distribution or water diffusion [7–9]. As far as we know, a general model taking
70 into account the different types of heat exchange between the system and the air, the transport
71 of water in the material and the evaporation from the water surface is missing in the literature.

72 In this work, we developed a model based on experimental results obtained under strictly
73 controlled conditions, using a mimosa tannin foam that we have synthesised and used to
74 improve water evaporation. Two cases were experimented, with and without insulation
75 around the vessel containing the water to be evaporated, to limit heat exchange at the
76 boundaries. These two cases were simulated, as the physics at the boundaries are different,
77 and were validated using the same model apart from the system geometry and a few
78 parameters. Various cases from the open literature have also been considered, allowing the
79 effects of various operating conditions and materials geometry to be explored, and to which
80 our model has been applied. Although the results between the literature experiments and our

81 simulations cannot be directly compared due to the different materials used, the main trends
82 could be successfully compared.

83 Therefore, our model should be particularly interesting in revealing the optimal geometry
84 parameters, such as the dimensions of the insulation to be used beneath a material, or to study
85 the impact of the insulation provided by synthetic foams used to allow the flotation of the
86 material. Prior to our research, a guideline for the main experimental conditions, such as
87 ambient temperature, relative humidity, geometry or position of the different elements, had
88 been discussed [10]. Here, these conditions are investigated to describe their impact on the
89 final evaporation rate and efficiency results, as our model takes into account the ambient air
90 temperature, relative air humidity, air convection type and solar flux.

91 **2 Materials and Methods**

92 **2.1 Evaporation material**

93 Firstly, a bio-based foam was prepared, from which water evaporation experiments were
94 conducted to validate our model. This foam was synthesised from tannin, a natural extract
95 from the bark of the mimosa tree (*Acacia Mearnsii*), using a process described elsewhere
96 [11]. The material was obtained by physical foaming, which involves producing a gas *in situ*
97 in a thermosetting resin during its polymerisation. **Table 1** shows all the ingredients used in
98 the process, indicating their relative amounts and their role in the formulation. Briefly, tannin
99 is first dissolved in water under magnetic stirring and then mixed with furfuryl alcohol. Next,
100 diethyl ether and a 37 wt. % aqueous solution of formaldehyde are added and the mixture is
101 carefully homogenised. Finally, a 65 wt. % aqueous solution of para-toluenesulphonic acid
102 (pTSA) is added under stirring, after which the mixture expands rapidly while polymerising at
103 the same time. Once fully expanded and cured, the foam is dried at room temperature for one
104 week; further details are given elsewhere [12]. The foam is then cut to the proper dimensions,
105 as shown in **Fig. 1** (about 58 mm in diameter and 15 mm thick).

106

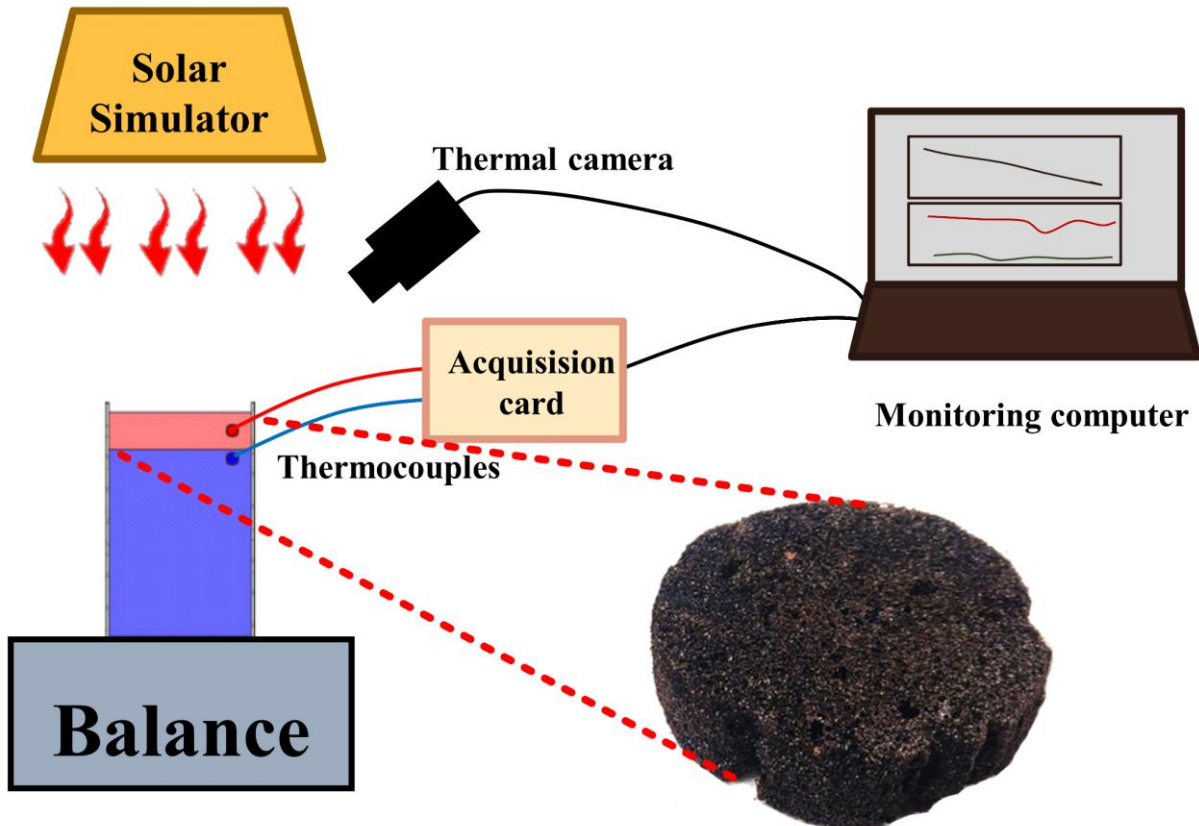
107 **Table 1.** Standard formulation of tannin-based foam.

Ingredients	Role in the formulation	Mass (g)
Mimosa tannin extract	Base of the resin	60
pTSA (65 wt. % in water)	Acidic catalyst	22
Furfuryl alcohol	Co-monomer	21
Formaldehyde (37 wt. % in water)	Crosslinker	14.8
Water	Solvent	12
Diethyl ether	Blowing agent	6

108

109 **2.2 Experimental protocol and measurement methods**

110 The experiment consists in illuminating a beaker (60 mm diameter), filled with tap water
 111 and with the foam floating on the surface, with a solar light simulator (SOLAR LIGHT LS-
 112 1000). The experimental setup is shown in **Fig. 1**. A Sartorius ENTRIS weighing scale
 113 accurate to the milligram is used to measure the mass of the whole system, and it is thus
 114 possible to determine the amount of evaporated water by difference. T-type thermocouples are
 115 used to measure temperatures at the interface between the evaporation material and the water
 116 on the one hand, and within the evaporation material on the other hand. A thermal camera
 117 (OPTRIS PI) pointing at the surface of the evaporation material is used to measure its
 118 temperature locally. Air temperature and relative humidity are measured using a sensor placed
 119 in the room. To explore the effect of heat exchange from the sides, a second experiment was
 120 also conducted with insulating foam around the beaker. Therefore, case 1 discussed below
 121 will refer to the case without insulation and case 2 to the case with insulation.



122

123 **Fig. 1.** Experimental setup used to measure the evaporation rate of water with a dark porous
 124 foam floating on the surface. The 15 mm-thick, 58 mm diameter tannin foam used for this
 125 purpose is shown in the lower right-hand corner.

126 In order to compare it with the numerical model, the experiment was carried out under
 127 three different solar concentrations: 0.7, 1.0 and 1.3 sun (1 sun being equal to 1 kW m^{-2}) for
 128 about one hour for each illumination. This allowed the evolution of heat and mass to be
 129 studied as a function of solar concentration. The system efficiency was calculated using Eq. 1:

$$\eta = \frac{\dot{m} h_v}{C_{opt} P_{s,0}} \quad \text{Eq. 1}$$

130 where \dot{m} ($\text{kg m}^{-2} \text{ h}^{-1}$) is the evaporation rate, C_{opt} (sun) is the solar concentration, and $P_{s,0}$
 131 (1000 W m^{-2}) is the power density of the average solar light on earth. Typical results in the
 132 literature present the evaporation rate and efficiency for a given specific solar power.
 133 Assuming a theoretical efficiency of 100 % and with 1 sun illumination contributing only to

134 the evaporation of water, whose enthalpy of vaporisation is 2450 kJ kg⁻¹ under STP
135 conditions, \dot{m} is equal to 1.47 kg m⁻² h⁻¹, which therefore represents the theoretical limit of
136 evaporation. Sometimes in the literature, evaporation in the dark is subtracted from the
137 evaporation rate with illumination to take into account only evaporation due to light. It is
138 useful to note that Eq. 1 does not take into account the heat exchange with the air, but only the
139 solar illumination input and the evaporation rate output. This is deliberate, as Eq. 1 is most
140 often used in the literature, and this is how we can compare our results with what has already
141 been published.

142 **3 Physical model**

143 A 2D axisymmetric model was written using COMSOL Multiphysics 5.6. Bulk water and
144 evaporation material were modelled as rectangles (in blue and red, respectively, in **Fig. 2**).
145 This basic geometry was adapted to cases 1 or 2 of the study, i.e., without or with an
146 insulating layer around the beaker, respectively. In this model, the upper surface is
147 illuminated by a solar radiation, is cooled by convection with air, and evaporates water. On
148 the sides and bottom, there are only convection and conduction, respectively.

149

150 **Fig. 2.** Types of heat exchange at the boundaries of the system: (a) case 1: without insulation;
151 and (b) case 2: with insulation.

152 **3.1 General equations**

153 In order to simulate the heat and mass transfers existing during the evaporation process,
154 energy and mass conservation equations were used to obtain the temperature, T , (Eq. 2) and
155 the volume fraction of liquid in the pores, ε_l (Eq. 3).

156 The conservation of energy equation describes conductive heat transfer and temperature
157 changes over time. The energy associated with mass transfer is small and due to the very slow
158 kinetics of this phenomenon, it has therefore been neglected in this study. This conservation
159 of energy equation is applied to calculate the temperature in the beaker and in the insulator
160 (corresponding to case 2).

$$\rho_j c_{p,j} \frac{\partial T}{\partial t} + \vec{V}(-\lambda_j \vec{V}T) = 0 \quad \text{Eq. 2}$$

161 where ρ_j (kg m^{-3}) is the density, $c_{p,j}$ ($\text{J kg}^{-1} \text{ K}^{-1}$) is the heat capacity, and λ_j ($\text{W m}^{-1} \text{ K}^{-1}$) is the
 162 thermal conductivity of component j (water w , evaporation material m or insulating layer i).

163 The mass transfer is described by a phenomenon of water diffusion in the porous material
 164 and is not solved in water or in the insulated medium. A transient equation is used in order to
 165 allow the material to dry out and thus reduce surface evaporation when it is no longer
 166 saturated. The equation is obtained by keeping the water liquid inside the material (Eq. 3).

$$\rho_w \frac{\partial \varepsilon_l}{\partial t} + \vec{\nabla} \left(-D \frac{\varepsilon_l \rho_w \rho_w}{\varepsilon_s \rho_s} \vec{\nabla} \varepsilon_l \right) = 0 \quad \text{Eq. 3}$$

167 where ε_l (dimensionless) is the water volume fraction in the evaporation material, ε_s
 168 (dimensionless) is its skeleton volume fraction, ρ_w (kg m^{-3}) is the density of liquid water, ρ_s
 169 (kg m^{-3}) is the skeleton density of the evaporation material, and D ($\text{m}^2 \text{ s}^{-1}$) is the diffusion
 170 coefficient of water in the evaporation material.

171 **3.2 Boundary conditions**

172 In this section, the boundary conditions used are specified. It should be noted that thermal
 173 continuity conditions are used for the heat equation for all internal boundaries.

174 *3.2.1 Interface between the air and the material*

175 The heat exchange at the surface (Eq. 4) takes into account convection, incoming light
 176 radiation, as well as losses by emission and by water evaporation (**Fig. 2**). The latter involves
 177 the surface evaporation, \dot{m}_{surf} ($\text{kg m}^{-2} \text{ h}^{-1}$), multiplied by the energy consumed to raise the
 178 temperature of water and the enthalpy of vaporisation of water, h_v (J kg^{-1}).

$$-\vec{n} (-\lambda_m \vec{\nabla} T) = h_c (T_a - T) + \dot{m}_{surf} (h_v + c_{p,w} (T_{w,i} - T)) + P_{s,0} C_{opt} + E_m \sigma (T_a^4 - T^4) \quad \text{Eq. 4}$$

179 with λ_m ($\text{W m}^{-1} \text{ K}^{-1}$) the thermal conductivity of the evaporation material, h_c ($\text{W m}^{-2} \text{ K}^{-1}$) the
 180 convection coefficient at the surface, $c_{p,w}$ ($\text{J K}^{-1} \text{ kg}^{-1}$) the heat capacity of water, $T_{w,i}$ (K) the
 181 initial temperature of water, $P_{s,0}$ (1000 W m^{-2}) the standard solar surface power, C_{opt} (sun)

182 the solar concentration (used to achieve different values of solar power), E_m (dimensionless)
 183 the emissivity of the material and σ ($5.67 \times 10^{-8} \text{ W m}^{-2} \text{ K}^{-4}$) the Stefan-Boltzmann constant,
 184 and $-\vec{n}$ the unit vector normal to the boundary.

185 To calculate the convective heat transfer coefficient, the following equation was used:

$$h_c = \frac{\lambda_{air}}{L_c} Nu \quad \text{Eq. 5}$$

186 where L_c is the characteristic length of the surface (which corresponds to the diameter for the
 187 top surface and the height for the side), and Nu is the Nusselt number (plane surface
 188 assumption), which can be calculated as follows:

$$Nu_{forced,top} = 0.3387 \frac{P_r^{\frac{1}{3}} R_e^{\frac{1}{2}}}{\left(1 + \frac{0.0468^2}{P_r}\right)^{\frac{1}{4}}} \quad \text{Eq. 6}$$

189 In Eq. 6, Re is the Reynolds number and Pr the Prandtl number, such that:

$$Pr = \frac{\mu}{\alpha} \quad \text{Eq. 7}$$

190 in which α is the thermal diffusivity and μ the dynamic viscosity of the fluid, here the air. The
 191 Reynolds number is calculated using the following equation:

$$Re = \frac{u L_c}{v} \quad \text{Eq. 8}$$

192 with u the velocity of air (m.s^{-1}) and v is kinematic viscosity ($\text{m}^2 \cdot \text{s}^{-1}$).

193 Since h_c is fitted for the case without any forced convection, the Nusselt number for the
 194 case of natural convection, $Nu_{natural}$, is determined using Eq. 5. Then, a Nusselt number
 195 $Nu_{combined}$, combination of both forced and natural convection, can be calculated [13]:

$$Nu_{combined} = (Nu_{natural}^4 + Nu_{forced}^4)^{\frac{1}{4}} \quad \text{Eq. 9}$$

196 At the upper surface, the water loss in the diffusivity equation is equal to the evaporation
 197 rate:

$$-\vec{n} \left(-D \frac{\varepsilon_l \rho_w \rho_w}{\varepsilon_s \rho_s} \vec{\nabla} \varepsilon_l \right) = \dot{m}_{surf} \quad \text{Eq. 10}$$

198 Finally, since water evaporation comes from the difference between the mass concentration of
 199 the surface and the air, then \dot{m}_{surf} is calculated as follows [14]:

$$\dot{m}_{surf} = -k_m \frac{M}{R} \left(\frac{P_w^{v,sat}}{T} a_w - H_R \frac{P_a^{v,sat}}{T_a} \right) \quad \text{Eq. 11}$$

200 where M (18×10^{-3} kg mol $^{-1}$) is the molar mass of water, R (8.314 J mol $^{-1}$ K $^{-1}$) is the universal
 201 gas constant, $P_w^{v,sat}$ (Pa) and $P_a^{v,sat}$ (Pa) are the water vapour pressures at the local
 202 temperature T (K) and at the air temperature T_a (K), respectively, a_w is the water activity, H_R
 203 (%) is the relative humidity and k_m (m s $^{-1}$) is the convective mass exchange coefficient,
 204 calculated using the Colburn analogy [13]:

$$k_m = \frac{h_c}{1000} \quad \text{Eq. 12}$$

205 $P_w^{v,sat}$ and $P_a^{v,sat}$ are calculated from the Clapeyron formula as follows:

$$P_x^{v,sat} = P_0 \exp \left(\frac{h_v}{R} M \left(\frac{1}{T_0} - \frac{1}{T} \right) \right) \quad \text{Eq. 13}$$

206 where $P_x^{v,sat}$ is the water vapour pressure at the temperature of the environment, P_0 is the
 207 standard pressure of 101 325 Pa and T_0 is the boiling point of water (373.15 K).

208 3.2.2 Interface between the air and the side of the system

209 Heat exchange between the air and the wall of the beaker involves convection and
 210 radiation losses:

$$-\vec{n} (-\lambda_j \vec{\nabla} T) = h_{c,s} (T_a - T) + E_s \sigma (T_a^4 - T^4) \quad \text{Eq. 14}$$

211 where λ_j (W m $^{-1}$ K $^{-1}$) has the same meaning as in Eq. 1, $h_{c,s}$ (W m $^{-2}$ K $^{-1}$) is the convection
 212 coefficient at the side, and E_s (dimensionless) is the emissivity of the side.

213 For forced convection at the side of the system, the following Nusselt expression is used
 214 assuming a vertical cylinder:

$$Nu_{forced,side} = 0.3 + \frac{0,62R_e^{1/2}P_r^{1/3}}{\left[1 + (0,4/P_r)^{\frac{2}{3}}\right]^{1/4}} \left[1 + \left(\frac{R_e}{282}\right)^{5/8}\right]^{4/5} \quad \text{Eq. 15}$$

215 *3.2.3 Interface between the weighing scale and the bottom of the beaker*

216 At the interface between the weighing scale and the bottom of the beaker, only a
 217 convective heat flow was assumed, formalised by:

$$-\vec{n}(-\lambda_w \vec{V}T) = h_{c,b}(T_a - T) \quad \text{Eq. 16}$$

218 where $h_{c,b}$ ($\text{W m}^{-2} \text{K}^{-1}$) is the convection coefficient at the bottom.

219 *3.2.4 Interface between the water and the evaporation material*

220 At the interface between the water and the evaporation material, as the latter is considered
 221 saturated, the liquid fraction is fixed at a value equal to the porosity, φ , and thermal continuity
 222 is assumed, i.e.:

$$\varepsilon_l = \varphi \quad \text{Eq. 17}$$

223 **3.3 Simulation parameters**

224 Table 2 lists the input parameters used in the simulation, and their symbols, definitions,
 225 units and values considered are also given.

226 **Table 2.** Input parameters used in the simulation.

Symbols	Definitions	Units	Values
$\lambda_w, \lambda_s, \lambda_a, \lambda_i$	Thermal conductivities of water, skeleton of the evaporation material, air, insulating material	$\text{W m}^{-1} \text{K}^{-1}$	0.6, 0.32, 0.0262, 0.043
φ	Porosity of the evaporation material	-	0.955
$c_{p,w}, c_{p,s}, c_{p,i}$	Heat capacities of water, evaporation material and insulating material	$\text{J K}^{-1} \text{kg}^{-1}$	4180, 1800, 871
D	Coefficient of diffusion of water inside the material	$\text{m}^2 \text{s}^{-1}$	10^{-8}
ρ_w, ρ_s, ρ_i	Density of water, skeleton density of the evaporation material, and bulk density of the insulating material	kg m^{-3}	1000, 1550, 30

σ	Stefan-Boltzmann constant	$\text{W m}^{-2} \text{K}^{-4}$	5.67×10^{-8}
R	Universal gas constant	$\text{J mol}^{-1} \text{K}^{-1}$	8.314
M	Molar mass of water	kg mol^{-1}	0.01801
P_0	Standard pressure	Pa	101325
T_0	Boiling point of water	K	373.15
$h_c, h_{c,s}, h_{c,b}$	Heat transfer coefficients at the surface, the side and the bottom	$\text{W m}^{-2} \text{K}^{-1}$	5, 5, 1
E_m, E_s	Emissivities of the material and of the side of the beaker	-	0.8, 0.8

227 3.3.1 Water activity

228 **Fig. 3** shows the water activity, a_w , as a function of water uptake (wt.%). a_w was obtained
229 from the experimentally obtained moisture sorption isotherm, taken from a previous study
230 [15], and corresponds to the partial vapour pressure of water divided by the standard vapour
231 pressure of water. From the knowledge of the moisture content inside the material, it was
232 possible to obtain the partial vapour pressure of water with the water activity, and thus to
233 calculate the evaporation rate using Eq. 11. Since the evaporation rate is related to the amount
234 of water at the surface, the WES performance is limited if there is not enough water at the
235 surface. At 31% water uptake, the water activity is 1, and remains constant for higher water
236 uptakes.

237

238 **Fig. 3.** Water activity in the tannin foam as a function of water uptake (after data from [15]).

239 3.3.2 *Thermal conductivity*

240 Since the porous evaporation material is partially filled with water, its average thermal
241 conductivity λ_m ($\text{W m}^{-1} \text{K}^{-1}$) must be calculated taking into account the thermal conductivities
242 of the material skeleton, water and air:

$$\lambda_m = \lambda_w \varepsilon_l + \lambda_s \varepsilon_s + \lambda_a \varepsilon_g \quad \text{Eq. 18}$$

243 where ε_s is the volume fraction of solid in the porous evaporation material, ε_g is the
244 corresponding volume fraction of gas such that $\varepsilon_g = 1 - \varepsilon_s - \varepsilon_l$, and λ_w , λ_s and λ_a (W m^{-1}
245 K^{-1}) are the thermal conductivities of water, material skeleton and air.

246 3.3.3 *Heat capacity*

247 The mass heat capacity of the material, $c_{p,m}$, varies much with the presence of water but
248 the effect of air on $c_{p,m}$ can be neglected. Therefore, the volumetric heat capacity was
249 calculated as follows:

$$\rho_m c_{p,m} = \varepsilon_l \rho_w c_{p,w} + \varepsilon_s \rho_s c_{p,s} \quad \text{Eq. 19}$$

250 where ρ_m (kg m^{-3}) and $c_{p,m}$ ($\text{J kg}^{-1} \text{K}^{-1}$) are the density and the mass heat capacity of the
251 simulated material filled with water, respectively, and $c_{p,s}$ ($\text{J kg}^{-1} \text{K}^{-1}$) is the mass heat
252 capacity of the dry, porous, evaporation material.

253 3.3.4 *Vaporisation enthalpy*

254 The enthalpy of vaporisation of water, h_v (kJ kg^{-1}), changes slightly with the temperature
255 according to [16]:

$$h_v = 1.91846 \times 10^3 \left(\frac{T}{T - 33.91} \right)^2 \quad \text{Eq. 20}$$

256 3.3.5 Numerical model

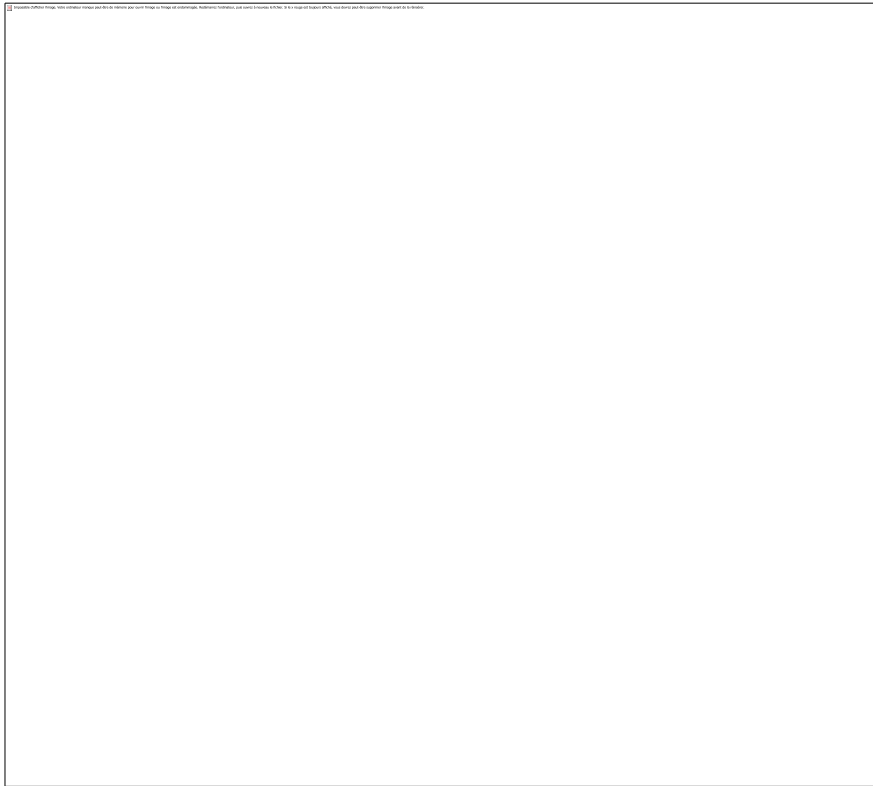
257 Calculated variables T and ε_l were obtained using the commercial software COMSOL
258 Multiphysics 5.6. First, a preliminary parametric study on the triangular mesh was carried out
259 in the first study case (*i.e.*, without insulation) for three meshes comprising 2569 elements
260 (mesh #1), 2873 elements (mesh #2), and 5553 elements (mesh #3). Since the impact of mesh
261 size on the results were extremely limited, mesh #2 with 2873 elements was used. **Fig. 4a**
262 shows a mesh consisting of 2873 elements for the first study case and 5431 for the second
263 (**Fig. 4b**), both refined at the interfaces between water and evaporation material, as well as the
264 interface between air and the evaporation material, with 100 elements. The rest of the mesh is
265 created automatically by the software, depending on the physics involved. Using a desktop
266 computer with a quad-core Xeon E5 coupled with 64 GB of RAM, the model for a system
267 without insulation is calculated in 1 minute and 5 seconds, while the model for a system with
268 insulation around the beaker is calculated in around 1 minute and 40 seconds. The simulation
269 required 90 calculation steps, with a step time self-determined by the software.

270

271 **Fig. 4.** Mesh used for the water evaporation system: (a) without insulation (case 1); and (b)
272 with insulation (case 2).

273 **4 Results and discussion**

274 In order to validate the numerical model, the results of the calculations were compared
275 with the results of the experiments obtained with the floating tannin-based foam, for the two
276 cases, i.e., with and without insulation foam. Then, different cases from the open literature
277 were examined with the proposed model, and the model was modified if necessary, taking
278 into account the different parameters considered in these former studies. This includes
279 ambient air temperature, relative humidity, solar power density, convection coefficient, and
280 system geometry. Overall, the objective is not to reproduce the same results from the
281 literature but to compare trends.



282 **4.1 Validation of the model**

283 Evaporation experiments were conducted without and with insulation (i.e., corresponding
284 to case 1 and 2, respectively) around the beaker containing the floating tannin foam, under
285 different solar inputs. To validate the simulation, the external conditions were imported as
286 input (T_a and H_r) and the duration was set to that of the experiment. The sunlight power was
287 set to three different values during the same test: 0.7 sun, then 1 sun and finally 1.3 sun, each
288 for a duration of 3300 seconds for the non-insulated configuration and 3500 seconds for the
289 insulated configuration. Changing the illumination in the middle of the test allows the
290 evolution over time of parameters such as temperature and mass loss to be validated when the
291 power input changes. The results of the simulation were compared to the average of three
292 experiments and are shown in **Fig. 5**.

293 *4.1.1 Non-insulated configuration*

294 **Fig. 5a** shows the vertical section of the configuration without insulation, where 1, 2 and 3
295 are the temperature measurement points, and **Fig. 5b** and **Fig. 5c** show the experimental and
296 predicted results.

298 **Fig. 5.** Revolution cross-section of the model water evaporation system in the case where this
299 system is (a) non-insulated, and (d) insulated; experimental (circles) and simulated (lines)
300 temperatures for (b) non-insulated and (e) insulated system; and water mass evolution for the
301 (c) non-insulated, and (f) insulated system.

302 The experimental evaporation rates are equal to 0.51, 0.70 and 1.01 $\text{kg m}^{-2} \text{ h}^{-1}$ with
303 efficiencies of 49, 47 and 52 % for 0.7, 1 and 1.3 sun, respectively. In comparison, the
304 calculated evaporation rates are equal to 0.48, 0.74 and 1.03 $\text{kg m}^{-2} \text{ h}^{-1}$ with efficiencies of 46,
305 50 and 53 % for 0.7, 1 and 1.3 sun, respectively. The difference between the simulated mass
306 of water and the experimental measurements is no higher than 5% (see **Fig. 5c**). The three
307 different solar inputs are clearly visible on the temperature curves, showing three successive
308 jumps. The agreement between measured and calculated temperatures is better in the
309 evaporation material (point 2) and at the interface between the latter and the water (point 3)
310 than at the surface (point 1) (see **Fig. 5b**). This discrepancy at point 1 is attributed to the
311 setting of the thermal camera (position, emissivity, measurement area) and the estimation of
312 fitted parameters in the model such as the convection coefficient. The average differences

313 between the simulated and experimental temperatures in the first case study are indeed, from
314 top to bottom, 1.01, 0.69 and 0.44 °C, which shows that the model reproduces the experiment
315 fairly closely.

316 *4.1.2 Insulated configuration*

317 **Fig. 5d, e and f** are equivalent to **Fig. 5a, b and c**, respectively, the only difference being
318 the layer of insulating material around the beaker. The experimental evaporation rates are
319 equal to 0.56, 0.82 and 1.19 kg m⁻² h⁻¹ with efficiencies of 53, 55 and 61 % for 0.7, 1 and 1.3
320 sun, respectively. In comparison, the calculated evaporation rates are equal to 0.54, 0.88 and
321 1.25 kg m⁻² h⁻¹ with efficiencies of 52, 59 and 64 % for 0.7, 1 and 1.3 sun, respectively. The
322 average difference between experimental and simulated masses of water is 8%, so it is higher
323 than in the non-insulated configuration. The differences for the three temperatures were 2.71,
324 1.31 and 0.64 °C for points 1, 2 and 3, respectively (**Fig. 5d**). As in the previous case (**Fig.**
325 **5b**), and for the same reasons, the difference between experimental and simulated surface
326 temperature is higher (point 1 in **Fig. 5d**) than for the other two temperatures, in the bulk
327 (point 2) and at the interface (point 3), which were recorded with thermocouples. However,
328 the evolution of the water mass over time is fairly well predicted by the model for the three
329 illuminations tested, as well as the transient thermal evolution that occurs when the input
330 sunlight changes.

331 The numerical model has therefore been validated and we can conclude that it can be used
332 to simulate water evaporation in the following. This validation was done on the basis of the
333 results obtained with tannin foam, but this material did not show particularly interesting
334 performances compared to other materials reported in the literature, and for which the
335 evaporation rate were close to 1.3 kg m⁻² h⁻¹ [17]. We now extend the application of this
336 model to these more efficient materials in terms of solar evaporation.

337 **4.2 Study of different cases using the model**

338 Among the large number of evaporation results for different materials and systems in the
339 literature, some phenomena and techniques are discussed repeatedly. The aim of this section
340 is to test the behaviour of our model when applied to the cases seen in the literature. Those
341 cases can be a good source of inspiration for the design of an efficient evaporation system.
342 For all studies considered, unless otherwise specified, the temperature of the air was set at 20
343 °C with a relative humidity (H_R) of 50 %. The initial temperature of all components was also
344 set at 20 °C.

345 *4.2.1 Impact of ambient conditions*

346 The previous section 4.1.2 has shown the significant impact of the beaker insulation on the
347 system performance, which indicates a dependence of the performance on the ambient
348 conditions. In order to better understand their impact, several parametric studies on the
349 exchanges between the air and the material (i.e., air temperature, relative humidity,
350 convection and solar input) were carried out using the numerical model. The evaporation
351 performance was calculated from the final results, which correspond to a steady state.

352 *4.2.1.1 Air temperature*

353 The first parameter that has an impact on the evaporation rate is the ambient air
354 temperature, which can be easily measured and controlled. In the simulation, we set the
355 relative humidity at 50 % with natural convection, and a parametric study was conducted on
356 the air temperature.

357 **Fig. 6a** shows the simulated evaporation rates for different values of air temperature, and
358 the corresponding evaporation efficiency. With increasing temperature, the evaporation rate
359 increases significantly, leading to changes of about $0.15 \text{ kg m}^{-2} \text{ h}^{-1}$ and 10 % efficiency for a
360 temperature change of 10 °C, which may be a reasonable change over a whole day.

361 Evaporation in the dark is also likely to change, as it is also shown in the same figure for three
362 different temperatures (taken from [4]).

363

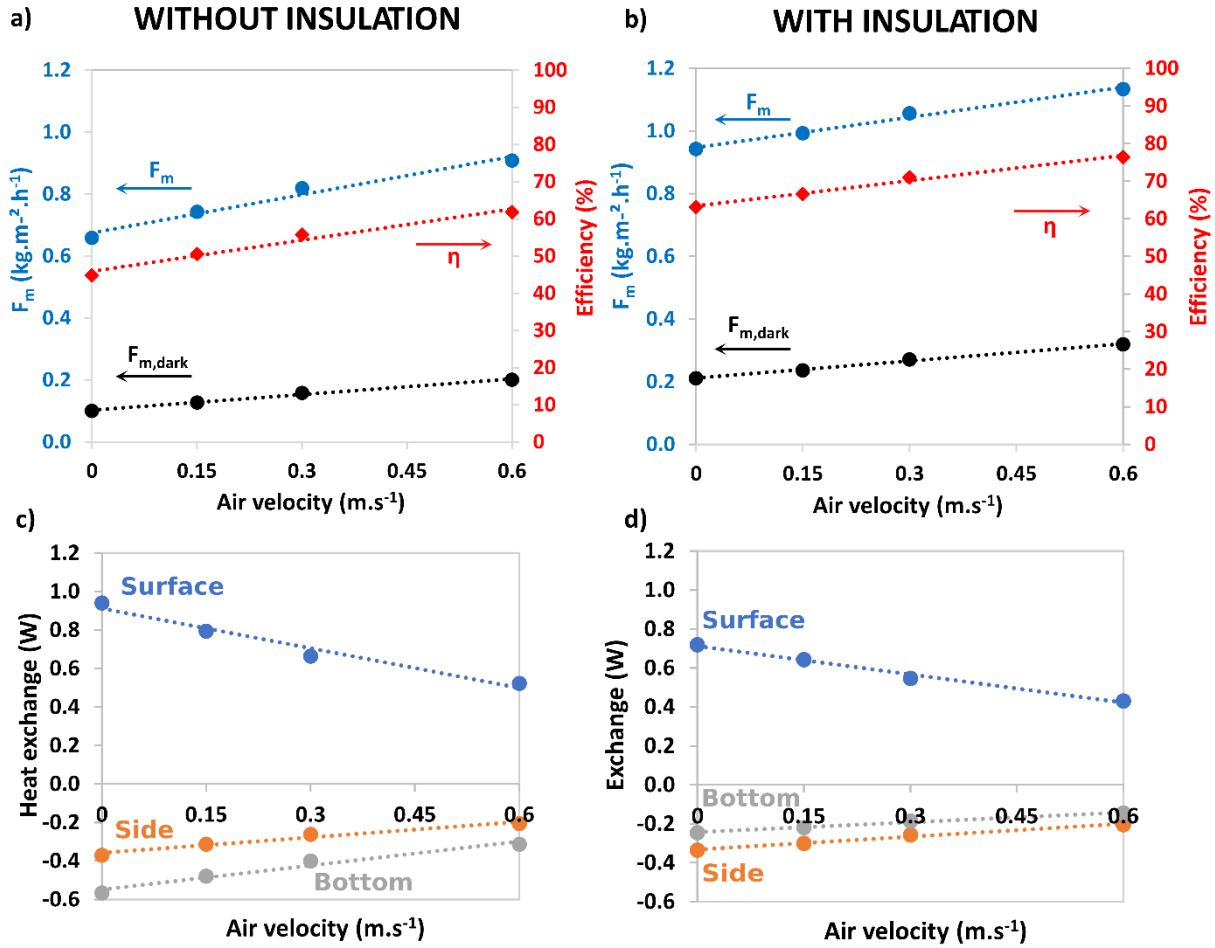
364 **Fig. 6.** Simulated evaporation rate as a function of: (a) air temperature at 50% H_R , with the
365 corresponding experimental evaporation in the dark (taken from [4]); and (b) relative
366 humidity of the air at 20 °C. In each case, some data of experimental evaporation rate in the
367 dark are also given: (a) at 3 different temperatures at 50% H_R ; and (b) at 3 different H_R at 23.6
368 °C (from [4]).

369 4.2.1.2 Relative humidity

370 The relative humidity (H_R) is considered in Eq. 11 and it also has an impact on the
371 evaporation rate at 20 °C, which was studied by varying the H_R from 10 to 90 %, with a 10 %
372 step. **Fig. 6b** shows the evaporation rate and efficiency as a function of H_R . Lower H_R
373 increases the evaporation rate and efficiency, for instance the evaporation rate increases from
374 0.60 kg m⁻² h⁻¹, with an efficiency of 40 % at 90% H_R , to 0.72 kg m⁻² h⁻¹, with an efficiency of
375 49% at 10 % H_R . Although H_R is a factor that has a significant impact on evaporation rate and
376 efficiency, it is easier to control and can simply be recorded as an ambient parameter. The
377 effect of H_R at 23.6 °C on the evaporation rate in the dark is also plotted for three H_R values
378 for reference (from [4]).

379 4.2.1.3 Heat exchange with air by convection

380 Insulating the system increases evaporation performance by increasing the temperature and
381 thus the evaporation rate [18], as shown when validating our model in section 4.1.2. Although
382 convection increases the heat exchange of the system with the air [19], which means that there
383 is more heat loss (Eq. 4, Eq. 14 and Eq. 16), convection also increases the evaporation rate F_m
384 (Eq. 11 and Eq. 12) with or without solar illumination. Here, three types of forced convection,
385 with and without insulation, are tested by adjusting the convection coefficients to three air
386 flow rates. These three flow rates are 0.15, 0.30 and 0.6 m s⁻¹ which corresponds to a heat
387 exchange coefficient at the evaporation surface h_c of 6.8, 9 and 12.4 W.m⁻².K⁻¹. **Fig. 7** shows
388 the surface evaporation rates in the dark and under 1 sun illumination with their
389 corresponding efficiencies as a function of the air flow rate, with and without insulation
390 around the beaker.



391

392 **Fig. 7.** Simulated evaporation rate: (a) without, and (b) with insulation for several air
 393 velocities. $F_{m,dark}$ and F_m are evaporation rates in the dark and under 1 sun, respectively.
 394 Heat exchange flux (such that losses take negative values) at different material surfaces: (c)
 395 without and (d) with insulation, as a function of air velocity.

396 Forced convection improves water evaporation performance in the dark and in the light,
 397 which means that although heat loss increases with convection, the evaporation rate benefits
 398 more. Insulation around the beaker also improves evaporation in darkness and light. Despite
 399 slightly reducing the slope of the trend line (compare **Fig. 7b** and **Fig. 7a**), beaker insulation
 400 gives the same results by increasing convection. As shown in **Fig. 1c** and **Fig. 7d**, the
 401 insulation reduces the amount of heat exchange between the material and the bulk water as
 402 well as between the material and its side, which is divided by 3 in the insulated case. The

403 global heat exchange between the air and the evaporation surface is lower in the insulated
404 case than in the non-insulated case. Considering that the solar input is the same, this is
405 consistent with the evaporation results. The more water evaporates, the more heat is
406 transferred to the air, and the less heat reaches the material surface. Overall, insulation can
407 only reduce the heat loss from the sides of the beaker, , which does not have as much impact
408 on evaporation as convection at the surface of the material. Nevertheless, convection may
409 improve evaporation in a large open area when a much larger evaporation surface is used, so
410 it is an interesting factor to consider when evaluating evaporation performance.

411 4.2.1.4 Solar power and efficiency

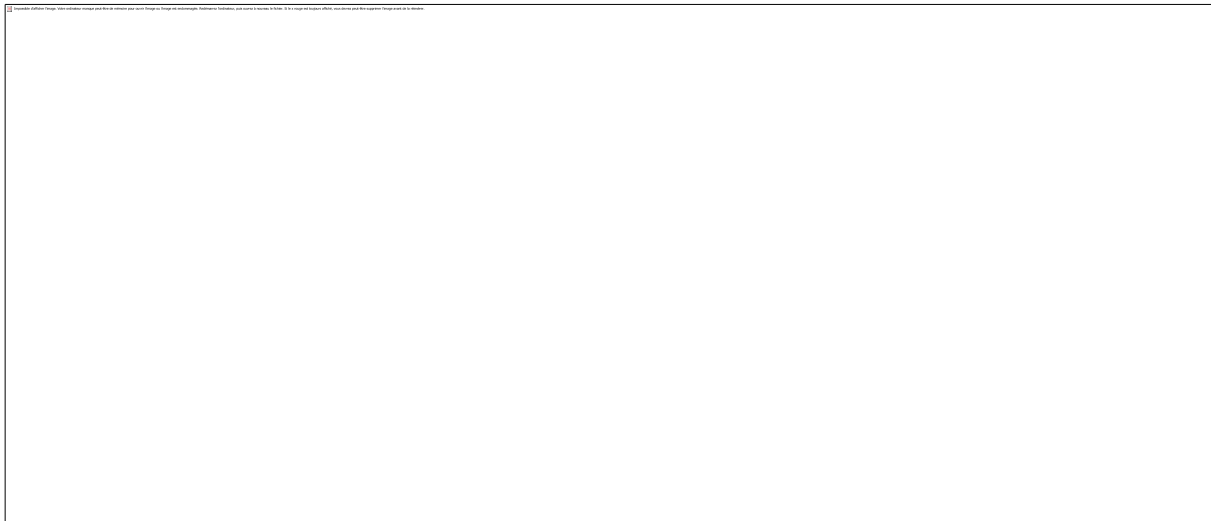
412 One of the most mentioned phenomena in the literature is the increase in evaporation
413 efficiency with increasing solar energy [20,21]. Many papers show results with illuminations
414 above 1 sun as solar energy input [22–28]. **Fig. 8** shows evaporation rate and efficiency
415 results from the literature as a function of solar power concentration. The more power there is
416 on the WES, the higher is the efficiency.

417

418 **Fig. 8** Evaporation rates (E.R.) and evaporation efficiencies for different solar concentrations,
419 as reported in the literature: (a) and (c) for a wood-based material [20] (reproduced from Ref.
420 [20] Copyright (2017), with permission from Wiley); and (b) and (d) for an improved
421 bamboo-based material [21] (reproduced from Ref. [21] Copyright (2020), with permission
422 from Elsevier).

423 Based on these articles, **Fig. 9a** shows the simulated evaporation rate and efficiency for our
424 system. The efficiency increases from 49 to 67 % when the illumination increases from 1 to 7
425 sun and so the evaporation rate increases from 0.7 to $6.9 \text{ kg m}^{-2} \text{ h}^{-1}$. It is important to note
426 that, according to Eq. 1, if the efficiency had remained constant, the evaporation rate at 7 suns
427 would have been $4.9 \text{ kg m}^{-2} \text{ h}^{-1}$ (only 7 times the evaporation at 1 sun). With a 15 % increase
428 in efficiency from 1 to 7 sun for our system, **Fig. 8c** showing a 12 % increase and **Fig. 8d** a 14

429 % increase for both systems from the literature, the increase in efficiency with the solar power
430 concentration is consistent.



431

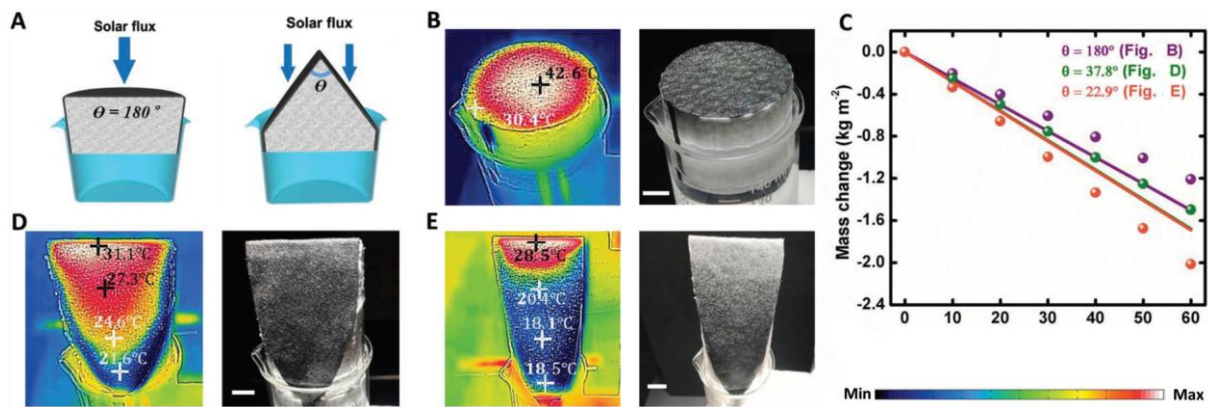
432 **Fig. 9** (a) Simulated evaporation rate and simulated efficiency for different solar
433 illuminations. (b) Evolution of the simulated evaporation rate F_m with surface temperature,
434 according to Eq. 11 and Eq. 13 (blue line), with the results of temperature and evaporation
435 rate at different solar illuminations (black dots).

436 Natural convection alone cannot be the only cause of the increase in efficiency and,
437 although the enthalpy of vaporisation also changes with the temperature according to Eq. 20,
438 it produces only a slight increase in the evaporation rate. The main cause of the increase in
439 efficiency is the surface temperature, which increases steadily with increasing illumination.
440 As $P_w^{v,sat}$ is a function of temperature (Eq. 13), the latter plays a major role in the evaporation
441 rate (Eq. 11). **Fig. 9b** shows that the evaporation rate increases exponentially with surface
442 temperature while it increased linearly with illumination (**Fig. 9a**).

443 *4.2.2 Increase of the exchange area with air*

444 Several studies have shown that increasing the evaporation area effectively increases the
445 performance of the system [4,7,29]. One of its consequences is a decrease in surface

446 temperature, due to the fact that sunlight is then scattered over a larger area and the exchange
 447 with air is higher, thus reducing the local heating and thus the temperature. This technique has
 448 already been explored in the literature [4], as shown in **Fig. 10**, with a carbon-coated paper
 449 placed on a polystyrene foam. By increasing the receiving area (**Fig. 10d** and **Fig. 10e**) the
 450 evaporation rate also increases (**Fig. 10c**).



451
 452 **Fig. 10** (a) Geometries used in the literature for increasing the exchange area; (b) surface
 453 temperature of the flat surface ($\theta = 180^\circ$); (c) experimental evaporation rate for the different
 454 surfaces (dots) and the theoretical limit of evaporation at 1 sun (lines); (d) surface temperature
 455 when $\theta = 37.8^\circ$; and (e) surface temperature when $\theta = 22.9^\circ$. Reproduced from Ref. [4]
 456 Copyright (2018).

457 Based on this work, we have modified the geometry of our model to represent the increase
 458 in surface area in the simulation. A conical geometry, not identical but close to the geometry
 459 illustrated in **Fig. 10a**, was chosen for its simplicity to be captured by the axisymmetric
 460 model. With such a geometry, we can easily conduct a parametric study on the height of the
 461 cone. For that purpose, a variable N has been created, which is written as follows:

$$N = \frac{h}{r} \quad \text{Eq. 21}$$

462 where h (m) and r (m) are the height and the radius of the base of the cone, respectively. This
 463 allows the cone height to be easily fixed in the simulation and to produce a parametric study
 464 with integer values. The solar power, initially 1 kW m^{-2} at the base of the cone, is decreased
 465 when the tip of the cone is stretched as this increases the area. A coefficient k (dimensionless)
 466 is defined to account for the corresponding scattering of the solar power. It represents the
 467 increase in surface area when changing from a flat surface to a conical surface and is
 468 calculated as follows:

$$k = \frac{S_{base}}{S_{cone}} = \frac{\pi r^2}{\pi r \sqrt{r^2 + (Nr)^2}} = \frac{1}{\sqrt{1 + N^2}} \quad \text{Eq. 22}$$

469 where S_{base} (m^2) is the area of the base of the cone and S_{cone} (m^2) is the lateral area of the
 470 cone. Therefore, the power concentration at the surface of the cone reads:

$$P_m = P_{s,0} k \quad \text{Eq. 23}$$

471 where P_m (kW m^{-2}) is the surface solar power arriving on the material, and $P_{s,0}$ (kW m^{-2}) is
 472 the surface solar power arriving from the sun. A with the decrease in power concentration, the
 473 evaporation rate increased, as the evaporation rate is still determined by the flat surface that
 474 receives the sunlight (S_{base}). **Fig. 11** shows the conical geometry used in the simulation with
 475 the parameters introduced previously, for three values of N . With the increase of the
 476 parameter N , k decreases, which reduces the solar power density.

477

478 **Fig. 11** Conical geometry used in the simulation, here shown for three parameters N : 0 (flat),
479 2 and 3.

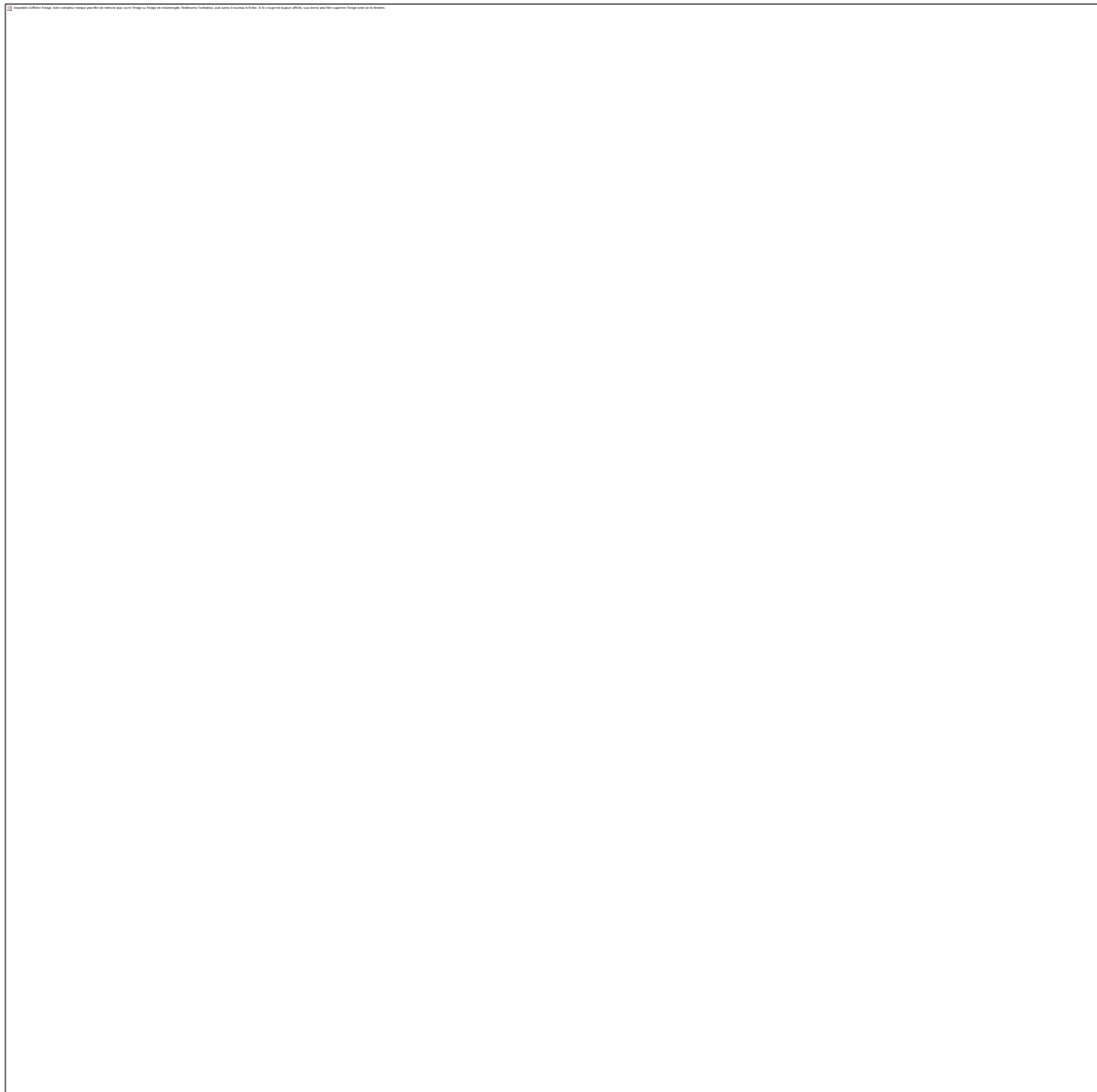
480 **Fig. 12a** shows the simulation results of evaporation rates and efficiencies by varying N
481 from $N = 0$ (flat surface) to $N = 8$, applying the model presented here. The temperatures are
482 also shown for each simulated cone. It can be observed that the evaporation rate and the
483 efficiency increase linearly with N while the surface temperature decreases. This observation
484 is contrary to the previous study, which showed that the evaporation flux increases with the
485 surface temperature. It can also be observed that the evaporation rate decreases with
486 increasing the area of the cone (**Fig. 12b**). The calculation of the performance of the system,
487 concerning evaporation, is not related to the exchange area but to the area at the base of the
488 structure. By calculating the flux related to the base, we observe an increase in the evaporated

489 flux as a function of N and therefore of the exchange area (**Fig. 12b**). It is also observed that
490 the ratio $1/k$ between the exchange area and the area at the base increases linearly with N (**Fig.**
491 **12c**), which shows the direct relationship between the evaporation area and the evaporated
492 flux related to the base of the cone. Overall, the increase in evaporation area is beneficial,
493 since it doubles the efficiency from $N = 0$ to 8, passing from 44 to 88%. It should be noted
494 that these efficiencies were calculated using Eq. 1, which does not take into account the heat
495 exchange with the air, but only the solar illumination input and the evaporation rate output.

496 However, such an improvement could have limitations, for example, a slender geometry
497 with $N = 8$ could be difficult to produce. Another possible geometry could be a recessed
498 spherical area, which might be easier to manufacture [30]. With such a geometry, the surface
499 allows the same kind of reduction of heat loss with air, but also a reduction of radiation loss,
500 since the light beam is partially reflected inside the sphere. Such a system could achieve 1.65
501 $\text{kg m}^{-2} \text{ h}^{-1}$ for a solar illumination of 1 sun [30].

502

503

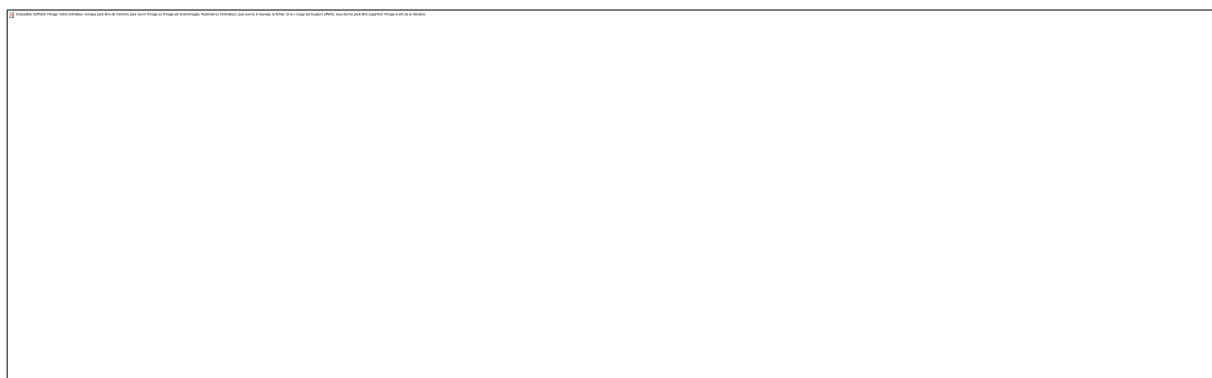


504

505 **Fig. 12.** (a) Simulated evaporation rate (left axis) and efficiency (right axis) calculated using
506 Eq. 1, for different values of N ($N = 0$ corresponding to a flat surface), and surface
507 temperature (colour bar code) as a function of geometry change; (b) evaporation rate
508 calculated with the base area as a reference and using the cone area as reference; and (c)
509 variations of k and $1/k$ with the increase of surface area.

510 *4.2.3 Insulation under the material*

511 Due to the natural shape of some materials, it is not possible to use them alone for
512 evaporation and therefore an additional material must be used to maintain the evaporative
513 surface above the water [5,31–35]. This can be a standard foam for thermal insulation, which
514 has the ability to float on water but also allows less heat exchange with water due to its very
515 low thermal conductivity. This was done by Xu et al. [31], whose system is shown in **Fig.**
516 **13a**, where a mushroom was placed on a polystyrene foam support. The path taken by the
517 water to evaporate is in the centre of the insulation foam, where a hole has been made to allow
518 the mushroom to touch the water. Similarly, **Fig. 13b** shows another type of WES that has
519 paper wrapped around an insulating foam [36] to allow water to be transported through the
520 sides of the system to an evaporation surface at the top.



521

522 **Fig. 13** (a) Mushroom-based water evaporation system on a floating polyurethane foam
523 support, reproduced with permission from Ref. [31]. Copyright 2017, Wiley-VCH; (b) a WES
524 using paper around an insulation foam, reproduced from Ref. [36]. Copyright (2016), with
525 permission from National Academy of Sciences.

526 Inspired by these two uses of insulating foam, we studied two configurations, one where
527 the insulator is located in the core of the evaporation material, with water transport taking
528 place at the sides, and the other where the insulator is located around the material, with water

529 transport taking place through a hole in the foam. These configurations are shown in **Fig. 14a**
530 and **Fig. 14b**, respectively.



531

532 **Fig. 14.** Simulated temperature of the system with the insulation layer located: (a) in the core,
533 with peripheral water transport, and (b) at the periphery, with a central hole for water
534 transport. Both configurations have the same radius and height ratio of the supporting foam to
535 the evaporation material.

536 Thus, the evaporation material is positioned on the insulating/floating foam, and water
537 transport is allowed either through a central hole or through the periphery. To study the
538 impact of the foam, parametric studies were conducted on the effects of varying the radius
539 (R_i) and the height (h_i) of the insulating foam. N_r and N_h represent the ratios of the radius and
540 heights of the foam to those of the evaporation material (see Eq. 24 and Eq. 25 and **Fig. 15**).

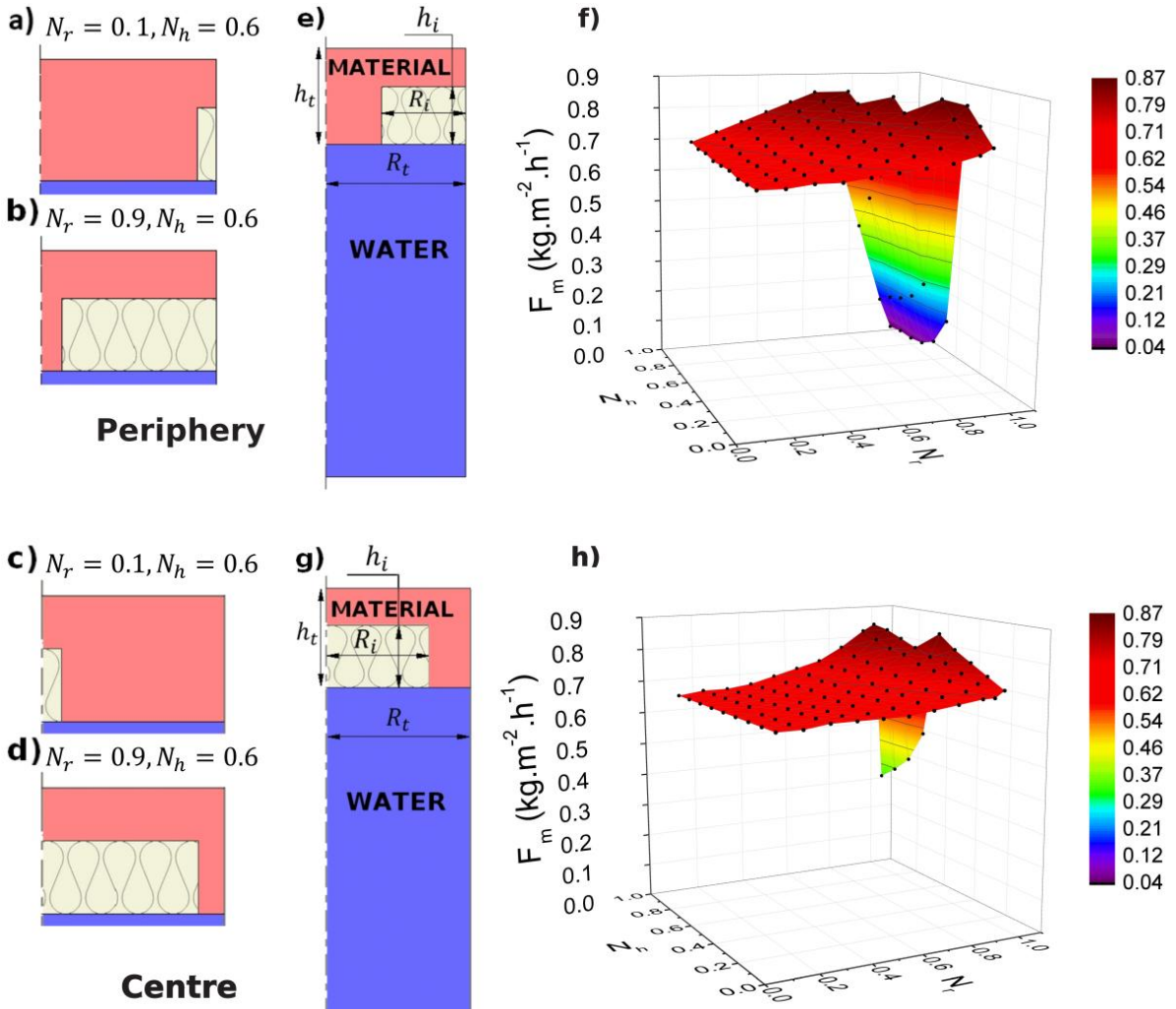
$$N_r = \frac{R_i}{R_t} \quad \text{Eq. 24}$$

$$N_h = \frac{h_i}{h_t} \quad \text{Eq. 25}$$

541 where R_t and h_t are the radius and the height of the evaporation material, respectively. The
542 higher N_h and N_r , the larger the foam and the more space it takes under the material. $N_r = 0$

543 with $N_h = 0$ thus correspond to the case without insulation layer. The variations of N_r for the
544 two configurations are represented in **Fig. 15**.

545 Adding an insulation layer under the evaporation material should theoretically improve
546 performance as more heat is retained on the surface. However, the addition of insulation
547 limits the transport of water to the surface, so a balance must be struck between heat and
548 water management. The simulation shows that increasing the size of the insulation, both in
549 radius and in height, increases evaporation to a certain point, where it reaches its maximum,
550 and then water transport limits the performance. The diffusion coefficient of water in the
551 evaporation material plays an important role in the dimensions of the insulation material that
552 can be used.



553

554 **Fig. 15.** Top: Cross-section of revolution of the evaporation system shown in **Fig. 14b** with
 555 insulation at the periphery for: (a) $N_r = 0.1$ and $N_h = 0.6$, and (b) $N_r = 0.9$ and $N_h = 0.6$; (e)
 556 system with its notations, and (f) results of evaporation rate for different values of N_r and N_h
 557 for insulation at the periphery. Bottom: Cross-section of revolution of the evaporation system
 558 shown in **Fig. 14a** for: (c) $N_r = 0.1$, and $N_h = 0.6$, and (d) $N_r = 0.9$ and $N_h = 0.6$; (g) system
 559 and its notations, and (h) results of evaporation rate for different values of N_r and N_h .

560 **Fig. 15a, b and e** show the simulation performed when insulation at the periphery was
 561 considered. **Fig. 15f** shows the increase in performance with the values of N_h and N_r , up to
 562 certain points where the insulation takes up too much space and therefore not enough water
 563 can be transported to the upper surface, thus limiting the evaporation rate. **Fig. 15c, d and g**

564 show the case of insulation in the centre. In this case, as shown in **Fig. 15h**, increasing the
565 size of the insulating foam in both directions increases the evaporation, and as in the first
566 case, up to a certain maximum after which it no longer increases. However, in this case, the
567 evaporation rate starts to decrease at higher values of N_h and N_r . This is due to the peripheral
568 transport of water, which spreads over a larger area compared to the hole in the centre.
569 Therefore, to obtain the same kind of proportion between the volume of the evaporation
570 material and the volume of the insulator, the radius of the insulating foam must be higher.
571 Nevertheless, this geometry, with a thin layer around the insulator, is limited by the
572 possibilities of preparation. A sheet of paper, like the one presented above, is feasible but a
573 foam-like product like our tannin foam would be impossible to cut so thin. Overall, the
574 peripheral insulation with $N_r = 0.9$ and $N_h = 0.4$ achieves an evaporation rate of $0.87 \text{ kg m}^{-2} \text{ h}^{-1}$
575 1 , while the central insulation with $N_r = 0.95$ and $N_h = 0.9$ gives $0.85 \text{ kg m}^{-2} \text{ h}^{-1}$.

576 These observations may be clues to making evaporation systems more efficient, since the
577 thermal conductivity of evaporation materials is strongly influenced by the amount of water
578 inside their porous structure. Having an additional insulating layer to prevent heat exchange
579 with water results in a higher evaporation rate, when water supply to the surface is not a
580 problem. However, this can also be an obstacle when comparing materials. Again, it is
581 essential to consider the whole system, with all the parameters and appropriate geometry, to
582 study its evaporation efficiency.

583

584 **5 Conclusion**

585 A two-dimensional axisymmetric model, validated for temperature and water mass
586 evolutions by experiments on a solar water evaporation system based on tannin foam, has
587 made it possible to study the impact of different operating parameters on the performance of
588 this type of system. As present, the tannin foam is of no interest in this type of system. This is

589 due to the fact that the open porosity of the foam is saturated with water, which considerably
590 limits its insulating properties.

591 We have shown that air temperature, relative air humidity and the type of air convection
592 around the system all have an impact on the evaporation rate. When the air temperature
593 increases from 20 to 50 °C, the evaporation rate is doubled, while a large change in relative
594 humidity has very little impact on performance. In addition, a system where the beaker is
595 insulated increases the performance of our material by 15 % on average, and increasing the
596 convection at the evaporation surface significantly increases the evaporated flux. This study
597 on the experimental conditions shows the need to approach the experimental conditions
598 recommended by Li et al. [10] with the air temperature of 25 °C and the relative air humidity
599 of less than 60 %, all in a breeze-free environment. Additionally, the cone study shows that
600 increasing the exchange area allows the evaporation rate of the system to be increased, which
601 is a considerable potential improvement for future development.

602 Finally, the addition of a thermal insulation layer to the evaporation material, with two
603 possible positions for the water transport channel, either at the centre or at the periphery of the
604 axisymmetric system, proved effective, providing good thermal insulation to prevent energy
605 from going to the water while not impeding water transport. With thermal insulation at the
606 periphery, N_r of 0.9 and N_h of 0.4 are the best parameters, while N_r of 0.95 and N_h of 0.9 is the
607 optimal combination when the insulation is in the centre of the system.

608 **Acknowledgements**

609 This study was supported by the TALiSMAN project, funded by ERDF (2019–000214).

610

611

612 **References**

- 613 [1] F. Zhao, Y. Guo, X. Zhou, W. Shi, G. Yu, Materials for solar-powered water
614 evaporation, *Nat. Rev. Mater.* (2020) 1–14. <https://doi.org/10.1038/s41578-020-0182-4>.
- 615 [2] P. Zhang, Q. Liao, H. Yao, Y. Huang, H. Cheng, L. Qu, Direct solar steam generation
616 system for clean water production, *Energy Storage Mater.* 18 (2019) 429–446.
617 <https://doi.org/10.1016/j.ensm.2018.10.006>.
- 618 [3] Y. Kuang, C. Chen, S. He, E.M. Hitz, Y. Wang, W. Gan, R. Mi, L. Hu, A High-
619 Performance Self-Regenerating Solar Evaporator for Continuous Water Desalination,
620 *Adv. Mater.* 31 (2019) 1900498. <https://doi.org/10.1002/adma.201900498>.
- 621 [4] H. Song, Y. Liu, Z. Liu, M.H. Singer, C. Li, A.R. Cheney, D. Ji, L. Zhou, N. Zhang, X.
622 Zeng, Z. Bei, Z. Yu, S. Jiang, Q. Gan, Cold Vapor Generation beyond the Input Solar
623 Energy Limit, *Adv. Sci.* 5 (2018) 1800222. <https://doi.org/10.1002/advs.201800222>.
- 624 [5] C. Zhang, P. Xiao, F. Ni, L. Yan, Q. Liu, D. Zhang, J. Gu, W. Wang, T. Chen,
625 Converting Pomelo Peel into Eco-Friendly and Low-Consumption Photothermic
626 Biomass Sponge Towards Multifunctional Solar-to-Heat Conversion, *ACS Sustain.*
627 *Chem. Eng.* (2020). <https://doi.org/10.1021/acssuschemeng.0c00681>.
- 628 [6] Q. Zhang, L. Ren, X. Xiao, Y. Chen, L. Xia, G. Zhao, H. Yang, X. Wang, W. Xu,
629 Vertically aligned *Juncus effusus* fibril composites for omnidirectional solar
630 evaporation, *Carbon*. 156 (2020) 225–233. <https://doi.org/10.1016/j.carbon.2019.09.067>.
- 631 [7] L. Wu, Z. Dong, Z. Cai, T. Ganapathy, N.X. Fang, C. Li, C. Yu, Y. Zhang, Y. Song,
632 Highly efficient three-dimensional solar evaporator for high salinity desalination by
633 localized crystallization, *Nat. Commun.* 11 (2020) 1–12. <https://doi.org/10.1038/s41467-020-14366-1>.
- 635 [8] F. Zhao, X. Zhou, Y. Shi, X. Qian, M. Alexander, X. Zhao, S. Mendez, R. Yang, L. Qu,
636 G. Yu, Highly efficient solar vapour generation via hierarchically nanostructured gels,
637 *Nat. Nanotechnol.* 13 (2018) 489–495. <https://doi.org/10.1038/s41565-018-0097-z>.
- 638 [9] Y. Guo, H. Lu, F. Zhao, X. Zhou, W. Shi, G. Yu, Biomass-Derived Hybrid Hydrogel
639 Evaporators for Cost-Effective Solar Water Purification, *Adv. Mater.* 32 (2020)
640 1907061. <https://doi.org/10.1002/adma.201907061>.
- 641 [10] X. Li, G. Ni, T. Cooper, N. Xu, J. Li, L. Zhou, X. Hu, B. Zhu, P. Yao, J. Zhu, Measuring
642 Conversion Efficiency of Solar Vapor Generation, *Joule*. 3 (2019) 1798–1803.
643 <https://doi.org/10.1016/j.joule.2019.06.009>.
- 644 [11] G. Tondi, V. Fierro, A. Pizzi, A. Celzard, Tannin-based carbon foams, *Carbon*. 47
645 (2009) 1480–1492. <https://doi.org/10.1016/j.carbon.2009.01.041>.
- 646 [12] Z. Marie, V. Nicolas, A. Celzard, V. Fierro, First approach for modelling the physical
647 foaming of tannin-based thermoset foams, *Int. J. Therm. Sci.* 149 (2020) 106212.
648 <https://doi.org/10.1016/j.ijthermalsci.2019.106212>.
- 649 [13] Y. CENGEL, Heat Transfer a practical approach, Second Edition, 2002.
- 650 [14] V. Nicolas, F. Vanin, D. Grenier, T. Lucas, C. Doursat, D. Flick, Modeling bread baking
651 with focus on overall deformation and local porosity evolution, *AIChE J.* 62 (2016)
652 3847–3863. <https://doi.org/10.1002/aic.15301>.

- 653 [15] C. Delgado-Sánchez, M. Letellier, V. Fierro, H. Chapuis, C. Gérardin, A. Pizzi, A.
654 Celzard, Hydrophobisation of tannin-based foams by covalent grafting of silanes, Ind.
655 Crops Prod. 92 (2016) 116–126. <https://doi.org/10.1016/j.indcrop.2016.08.002>.
- 656 [16] B. Henderson- Sellers, A new formula for latent heat of vaporization of water as a
657 function of temperature, Q. J. R. Meteorol. Soc. 110 (1984) 1186–1190.
658 <https://doi.org/10.1002/qj.49711046626>.
- 659 [17] R. Fillet, V. Nicolas, V. Fierro, A. Celzard, A review of natural materials for solar
660 evaporation, Sol. Energy Mater. Sol. Cells. 219 (2021) 110814.
661 <https://doi.org/10.1016/j.solmat.2020.110814>.
- 662 [18] Y. Wang, X. Wu, X. Yang, G. Owens, H. Xu, Reversing heat conduction loss:
663 Extracting energy from bulk water to enhance solar steam generation, Nano Energy. 78
664 (2020) 105269. <https://doi.org/10.1016/j.nanoen.2020.105269>.
- 665 [19] S. Ali, S.A.U. Rehman, H.-Y. Luan, M.U. Farid, H. Huang, Challenges and
666 opportunities in functional carbon nanotubes for membrane-based water treatment and
667 desalination, Sci. Total Environ. 646 (2019) 1126–1139.
668 <https://doi.org/10.1016/j.scitotenv.2018.07.348>.
- 669 [20] C. Sheng, N. Yang, Y. Yan, X. Shen, C. Jin, Z. Wang, Q. Sun, Bamboo decorated with
670 plasmonic nanoparticles for efficient solar steam generation, Appl. Therm. Eng. 167
671 (2020) 114712. <https://doi.org/10.1016/j.applthermaleng.2019.114712>.
- 672 [21] C. Chen, Y. Li, J. Song, Z. Yang, Y. Kuang, E. Hitz, C. Jia, A. Gong, F. Jiang, J.Y. Zhu,
673 B. Yang, J. Xie, L. Hu, Highly Flexible and Efficient Solar Steam Generation Device,
674 Adv. Mater. 29 (2017) 1701756. <https://doi.org/10.1002/adma.201701756>.
- 675 [22] Q. Jiang, L. Tian, K.-K. Liu, S. Tadepalli, R. Raliya, P. Biswas, R.R. Naik, S.
676 Singamaneni, Bilayered Biofoam for Highly Efficient Solar Steam Generation, Adv.
677 Mater. 28 (2016) 9400–9407. <https://doi.org/10.1002/adma.201601819>.
- 678 [23] M. Zhu, Y. Li, F. Chen, X. Zhu, J. Dai, Y. Li, Z. Yang, X. Yan, J. Song, Y. Wang, E.
679 Hitz, W. Luo, M. Lu, B. Yang, L. Hu, Plasmonic Wood for High-Efficiency Solar Steam
680 Generation, Adv. Energy Mater. 8 (2018) 1701028.
681 <https://doi.org/10.1002/aenm.201701028>.
- 682 [24] M. Zhu, Y. Li, G. Chen, F. Jiang, Z. Yang, X. Luo, Y. Wang, S.D. Lacey, J. Dai, C.
683 Wang, C. Jia, J. Wan, Y. Yao, A. Gong, B. Yang, Z. Yu, S. Das, L. Hu, Tree-Inspired
684 Design for High-Efficiency Water Extraction, Adv. Mater. 29 (2017) 1704107.
685 <https://doi.org/10.1002/adma.201704107>.
- 686 [25] Z. Li, M. Zheng, N. Wei, Y. Lin, W. Chu, R. Xu, H. Wang, J. Tian, H. Cui, Broadband-
687 absorbing WO₃-x nanorod-decorated wood evaporator for highly efficient solar-driven
688 interfacial steam generation, Sol. Energy Mater. Sol. Cells. 205 (2020) 110254.
689 <https://doi.org/10.1016/j.solmat.2019.110254>.
- 690 [26] M.M. Ghafurian, H. Niazmand, E. Ebrahimnia-Bajestan, R.A. Taylor, Wood surface
691 treatment techniques for enhanced solar steam generation, Renew. Energy. 146 (2020)
692 2308–2315. <https://doi.org/10.1016/j.renene.2019.08.036>.
- 693 [27] Z. Yu, S. Cheng, C. Li, Y. Sun, B. Li, Enhancing efficiency of carbonized wood based
694 solar steam generator for wastewater treatment by optimizing the thickness, Sol. Energy.
695 193 (2019) 434–441. <https://doi.org/10.1016/j.solener.2019.09.080>.

- 696 [28] N.S. Lewis, D.G. Nocera, Powering the planet: Chemical challenges in solar energy
697 utilization, Proc. Natl. Acad. Sci. U. S. A. 103 (2006) 15729–15735.
698 <https://doi.org/10.1073/pnas.0603395103>.
- 699 [29] S.-L. Wu, H. Chen, H.-L. Wang, X. Chen, H.-C. Yang, S.B. Darling, Solar-driven
700 evaporators for water treatment: challenges and opportunities, Environ. Sci. Water Res.
701 Technol. 7 (2021) 24–39. <https://doi.org/10.1039/D0EW00725K>.
- 702 [30] S. Li, Y. He, Y. Wang, D. Liao, H. Liu, L. Zhou, C. Wei, C. Yu, Y. Chen, Simple
703 Hierarchical Interface Design Strategy for Accelerating Solar Evaporation, Macromol.
704 Mater. Eng. n/a (n.d.) 2000640. <https://doi.org/10.1002/mame.202000640>.
- 705 [31] N. Xu, X. Hu, W. Xu, X. Li, L. Zhou, S. Zhu, J. Zhu, Mushrooms as Efficient Solar
706 Steam-Generation Devices, Adv. Mater. 29 (2017) 1606762.
707 <https://doi.org/10.1002/adma.201606762>.
- 708 [32] Z. Lin, T. Wu, J. Shi, B. Zhou, C. Zhu, Y. Wang, R. Liang, M. Mizuno, Poly(N-
709 phenylglycine)-Based Bioinspired System for Stably and Efficiently Enhancing Solar
710 Evaporation, ACS Sustain. Chem. Eng. 9 (2021) 448–457.
711 <https://doi.org/10.1021/acssuschemeng.0c07608>.
- 712 [33] Y. Liao, J. Chen, D. Zhang, X. Wang, B. Yuan, P. Deng, F. Li, H. Zhang, Lotus leaf as
713 solar water evaporation devices, Mater. Lett. 240 (2019) 92–95.
714 <https://doi.org/10.1016/j.matlet.2018.12.133>.
- 715 [34] M. Zhu, A. Xia, Q. Feng, X. Wu, C. Zhang, D. Wu, H. Zhu, Biomass Carbon Materials
716 for Efficient Solar Steam Generation Prepared from Carbonized Enteromorpha Prolifera,
717 Energy Technol. n/a (2019) 1901215. <https://doi.org/10.1002/ente.201901215>.
- 718 [35] X. Wang, C. Sha, W. Wang, Y. Chen, Y. Yu, D. Fan, Functionalized biomass-derived
719 composites for solar vapor generation, Mater. Res. Express. 6 (2019) 125613.
720 <https://doi.org/10.1088/2053-1591/ab586e>.
- 721 [36] X. Li, W. Xu, M. Tang, L. Zhou, B. Zhu, S. Zhu, J. Zhu, Graphene oxide-based efficient
722 and scalable solar desalination under one sun with a confined 2D water path, Proc. Natl.
723 Acad. Sci. 113 (2016) 13953–13958. <https://doi.org/10.1073/pnas.1613031113>.
- 724